JOURNAL OF GEOPHYSICAL RESEARCH, VOL. 117, C06015, doi:10.1029/2012JC007986, 2012

Origins of features in wave number-frequency spectra of space-time images of the ocean

William J. Plant[1] and Gordon Farquharson[1]

Received 15 February 2012; revised 2 May 2012; accepted 3 May 2012; published 20 June 2012.

[1] Wave number-frequency spectra measured with remote sensing systems consist of energy along the ocean wave dispersion relation and additional features that lie above and below this relation. At low frequencies a feature passing through the origin as a straight line is observed while one or more high-frequency features exhibit substantial curvature. Here we utilize images obtained on the open ocean from microwave Doppler shifts, which are directly related to scatterer velocity and allow us to calculate expected wave-wave interaction effects. We show that the strongest features lying off the first-order dispersion relation are not primarily due to second-order interactions, breaking caused by wind turbulence, advection by turbulence, or shadowing. The low-frequency feature can be seen traveling in the opposite direction to swell when looking nearly crosswind. We show that the most probable cause of these features is the interference of long ocean waves, which causes breaking near local maxima of surface slope. Doppler spectra observed by the radars indicate that the maximum speed reached by water particles on the open ocean is less than 6 m/s and usually close to the speed of the low-frequency feature in the wave number-frequency spectrum. Since this is much less than the phase speeds of dominant wind waves and swell, neither of these waves can be the breaking wave. Rather, we hypothesize that the superposition of these waves steepens short gravity waves on the surface, which then break to produce water parcels traveling near their phase speed, the speed observed by the radar.

Citation: Plant, W. J., and G. Farquharson (2012), Origins of features in wave number-frequency spectra of space-time images of the ocean, *J. Geophys. Res.*, *117*, C06015, doi:10.1029/2012JC007986.

1. Introduction

[2] Data from the ocean surface as a function of both space and time can be obtained by various remote sensing techniques with sufficiently high resolution to produce wave number-frequency spectra with little aliasing. Such spectra can be produced either by computing the two-dimensional Fourier transform of a space-time image along a given direction (usually averaged over some perpendicular distance) or by computing three-dimensional Fourier transforms of a time stack of two-dimensional spatial images. When either of these techniques is used, features at frequencies higher than the first-order dispersion relation and lower-frequency features passing in a straight line through origin can be seen in addition to the energy that resides along the first-order dispersion relation. Data can be obtained at optical, infrared, or microwave frequencies [*Frasier and McIntosh*, 1996; *Smith et al.*, 1996; *Stevens et al.*, 1999; *Dugan et al.*, 2001; *Dugan and Piotrowski*, 2003, 2012]. While the high-frequency features have generally been attributed to nonlinear wave-wave interaction effects, the low-frequency features have been explained by various means in addition to nonlinear wave effects. The explanations include a jet ski in the image [*Dugan et al.*, 2001], turbulent wind effects, fronts and foam patches advected by the current [*Dugan and Piotrowski*, 2003, 2012], breaking waves [*Frasier and McIntosh*, 1996; *Stevens et al.*, 1999], and nonlinear scattering effects [*Frasier and McIntosh*, 1996; *Rino et al.*, 1997; *Stevens et al.*, 1999]. In this paper we investigate the origins of these features as observed by a coherent, X-band microwave radar that was mounted on the R/V Thompson in the summer of 2008 on a cruise in deep water along the west coast of the United States. We will utilize images of the first moments of Doppler spectra in the analysis since these are insensitive to clipping in the electronics and data processing [*Van Vleck and Middleton*, 1966].

[3] We will first look at the possibility that the low-frequency feature in the spectrum is due to second-order nonlinear wave/wave interactions. Since the pioneering work of Phillips, Longuet-Higgins, and Hasselmann, the importance of nonlinear wave/wave interactions in the nature of surface water waves has been realized [*Phillips*, 1960;

[1]Applied Physics Laboratory, University of Washington, Seattle, Washington, USA.

Corresponding author: W. J. Plant, Applied Physics Laboratory, University of Washington, 1013 NE 40th St., Seattle, WA 98105-6698, USA. (plant@apl.washington.edu)

0148-0227/12/2012JC007986

Longuet-Higgins, 1962; *Hasselmann*, 1962]. Most work on nonlinear wave/wave interactions since then has concentrated on third-order (four-wave) interactions because they result in wave products that lie on the first-order dispersion relation in the wave number-frequency spectrum. Therefore these interactions cause energy to be transferred among spectral components and shift the phase speed of these components slightly from the first-order values [*Longuet-Higgins*, 1962; *Hasselmann*, 1963; *Barrick and Weber*, 1977]. However, second-order wave/wave interactions also exist and are pointed out in these works. These lie off the first-order dispersion relation in wave number-frequency space, and therefore do not cause energy transfer. They do, however, cause detectable effects on the surface displacement [*Weber and Barrick*, 1977]. Since the second-order products lie above and below the first-order dispersion relation in a wave number/frequency spectrum, and the low-frequency one passes through the origin, we investigate here whether these interactions can explain features that we have observed for upwind and downwind cases. We conclude that they cannot, both because they are too weak and because the resulting second-order spectral features are not located in the same position in wave number-frequency space as the observed features. Furthermore, we document features observed when looking nearly cross wind that cannot be reproduced by second-order wave-wave interactions. Based on these cross wind data and the observed mislocation of predicted second-order features, we will conclude that no second-order phenomenon, whether hydrodynamic or electromagnetic, can explain the features.

[4] We then look at other phenomena that could account for the features. We examine the possibility that shadowing causes the features of interest. We show that these features exist in microwave data collected at grazing angles well above those at which shadowing can exist. Thus shadowing cannot be the only cause of the features. In light of recent experimental results on the existence of geometric shadowing, we argue that shadowing is unlikely to be the cause of the features for data taken on the open ocean even at low-grazing angles (W. J. Plant and G. Farquharson, Wave shadowing and modulation of microwave backscatter from the ocean, submitted to *Journal of Geophysical Research*, 2012). We also show that the slope of the low-frequency feature in the spectrum implies that it is caused by something on the ocean surface moving much slower than the wind speed during our data collection periods, which shows that turbulent eddies traveling with the mean wind speed cannot cause the features. Finally, because the slope of the low-frequency feature is about 3.5 m/s in our data, much faster than oceanic currents, it cannot be caused by the advection of turbulence by currents as found in visible imagery of rivers and inlets by *Dugan and Piotrowski* [2003, 2012].

[5] Since swell and wind waves coexisted on the ocean at the time of the measurements, we propose that their interference pattern with each other and within the wind-wave system produce breaking waves that are responsible for both the low-frequency features and the other features that exist at frequencies higher than the first-order dispersion relation. We show that the interference of the swell and wind waves and within the wind wave system produce features in space/time images that match those seen in our radar imagery. Furthermore, the low-frequency feature travels at speeds that are comparable to the maximum speeds of water particles that show up in our Doppler spectra. Since these maximum speeds are well below the phase speeds of either the dominant wind waves or swell, we propose that they are produced by short gravity waves that travel with the interference pattern, are steepened by it, and break to produce water parcels that travel at very nearly their phase speeds.

2. The Experiment

[6] In August 2008, APL/UW operated its coherent, X-band radar, CORAR, onboard the R/V Thompson on a cruise along the northwest coast of the U.S.. In the shipboard configuration, CORAR had four parabolic antennas mounted on a partially stabilized, rotating mount and set at an incidence angle between 88° and 89°. The four antennas were directed 90° apart in azimuth and opposite pairs collected data on alternate pulses at a rate of 25 kHz for each antenna. A switch changed the pair of antennas being used every 41 ms. All antennas were vertically polarized on both transmit and receive. They were parabolic antennas with 3.5° half-power, one-way beam widths, yielding a two-way pattern 2.5° wide. The radar sampled backscatter sufficiently rapidly that complete Doppler spectra could be obtained at each of 256 range bins, which were 7.5 m wide in these experiments. From these Doppler spectra, zeroth, first and second moments were computed; the zeroth moments were converted to normalized radar cross sections through calibration [*Plant et al.*, 1998] while the first moments were converted to scatterer velocities and second moments yielded the spread of scatterer velocities. For each look direction, space/time images of both the normalized radar cross section and the scatterer velocity were formed. Only the images of scatter velocity are used here.

[7] Most data on this cruise were collected with the mount rotating. However, near the end of the cruise, the antennas were operated without rotation (or stabilization) for nearly a day and these are the data on which we concentrate in this paper. Under these circumstances space/time images could be collected with minimal aliasing. Figure 1 shows an example of an image and spectrum of scatterer velocity collected during the cruise with the antenna pointed into the wind at grazing angles near 1°. The first-order dispersion relation containing the spectral peak indicated by the arrow at a frequency of 0.162 Hz and a wave number of 0.0915 rad/m can be seen in Figure 1b. Our convention is that features lying in the first and third quadrants represent waves traveling toward the antenna. Therefore the dominant wave is a 6.19 s wave, 68.6 m long traveling at 11.1 m/s toward the antenna. Since a 68.6 m wave would have a period of 6.63 s and a speed of 10.35 m/s in the absence of current, these measurements indicate that a component of apparent current of about 0.75 m/s existed in the direction of wave, opposite the direction of ship travel. Since the ship moved at about 0.5 m/s, this implies a current component of about 0.25 m/s in the opposite direction of ship travel, that is, to the south.

[8] Waves of the dominant period and frequency are also obvious in Figure 1a. A clear modulation of these waves is evident in this space/time image. The modulation pattern has a speed of 3.6 m/s, which is not the group speed of the dominant wave, 5.2 m/s. Figure 1b shows two other features

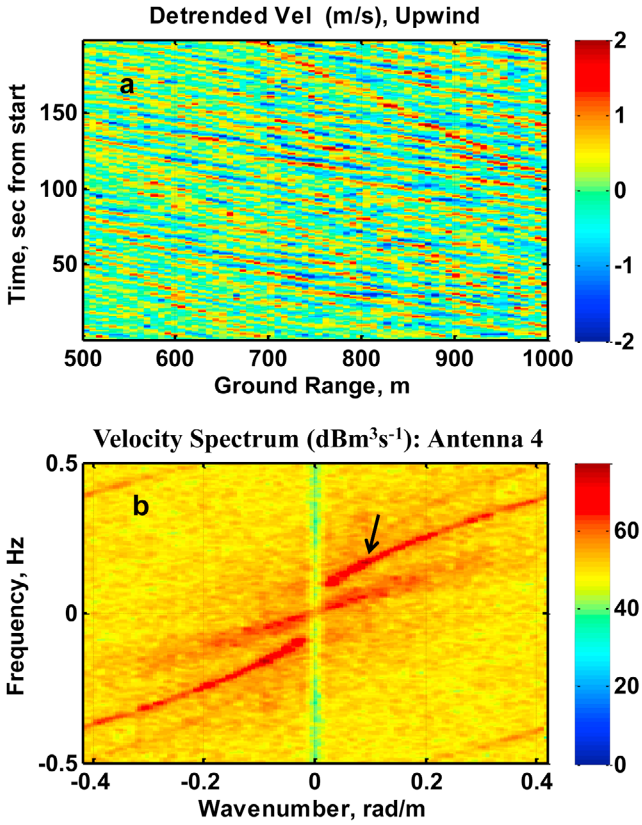

Figure 1. (a) Image of horizontal scatterer velocities obtained from a shipboard, coherent, X-band radar starting at 22:21:21 UTC on August 16, 2008. The polarization was VV. (b) The spectrum of this image showing first and possible second-order wave effects. The data have been detrended, as evidenced by the low spectral densities in b at zero wave number. The wind velocity was 7.5 m/s from 333°T, the ship velocity was 0.5 m/s to 346°T, and the antenna was looking toward 333°T, upwind. The slope of the linear feature through zero corresponds to a speed of 3.6 m/s. The arrow indicates the dominant wave peak.

of interest, the feature lying above the first-order dispersion and the nearly straight, low-frequency feature that goes through zero. The low-frequency feature has a speed of 3.6 m/s, consistent with the speed of the modulation pattern in the space/time image, but much smaller than the wind speed and larger than any possible current. This shows that this feature is not related to breaking caused by turbulent eddies in the wind traveling at the mean wind speed or to the advection of turbulence in the water due to currents.

[9] The data presented here can be considered to be nearly one-dimensional spatially for the following reasons. First, ocean wave spectra are well known to have a rather narrow angular spread at wave numbers near the dominant wave [*Donelan et al.*, 1985]. Second, the horizontal component of orbital wave velocity has a cosine fall-off with azimuth angle. Finally, the long, thin cell illuminated by the radar at each range bin discriminates against waves traveling away from the line of sight for all but the longest waves. For instance, this cell is 7.5 m in the range direction and 22 m long in the azimuth direction at a range of 500 m. The half-width at the 1/e point of the angular resolution of the antennas to a wave 68 m long is shown in Figure 2 as a function of range [*Plant et al.*, 1987]. Given this antenna response, we will compare our measured spectra to theoretical, one-dimensional, second-order wave/wave interactions.

3. Second-Order Water Waves

3.1. Perturbation Expansion

[10] To calculate second-order wave effects here, we will follow the work of *Weber and Barrick* [1977]. *Creamer et al.* [1989] pointed out that Weber and Barrick omitted a second-order term from their equations. However, the term that was omitted lies on the first-order dispersion curve and lowers the first-order spectral density by a small amount. Our object here is to interpret the spectral features that do not lie on the first order dispersion curve, so we use Weber and Barrick's result.

[11] As with all perturbation calculations of surface wave displacements, the calculations begin with the conservation, Navier-Stokes, and surface continuity equations. Following Weber and Barrick, wind and viscous effects are neglected. Then the three fundamental equations are

$$\text{Conservation of mass} \quad \nabla^2\varphi = 0 \tag{1}$$

$$\text{Navier-Stokes} \left[\frac{\partial\varphi}{\partial t} + \frac{1}{2}\nabla\varphi\cdot\nabla\varphi\right]_{z=\eta} = -g\eta \tag{2}$$

$$\text{Surface continuity} \left[\frac{\partial\varphi}{\partial z}\right]_{z=\eta} = \frac{\partial\eta}{\partial t} + [\nabla\eta\cdot\nabla\varphi]_{z=\eta} \tag{3}$$

Here g is gravitational acceleration, and the equations are evaluated at the surface since our interest is in the velocity and displacement of the surface. The surface displacement is represented by η in the above equations and φ is the velocity potential which is related to the velocity through $\mathbf{v} = \nabla\varphi$.

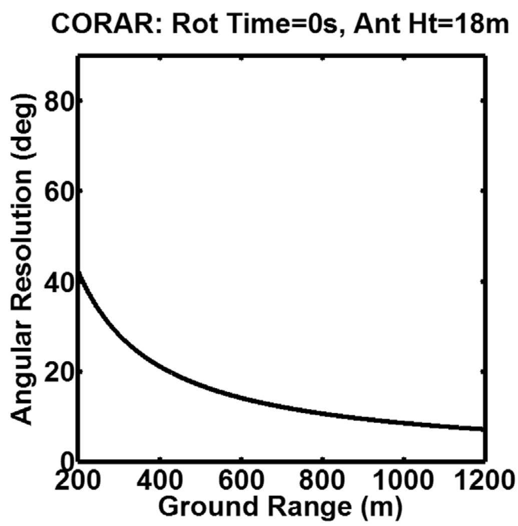

Figure 2. Angular resolution (half-width at 1/e point) of the CORAR parabolic antennas to a surface water wave 68 m long. The antennas are two feet in diameter and 18 m above the mean surface.

[12] To proceed, η and φ are expanded in Fourier series,

$$\eta(\mathbf{r},t) = \int \eta(\mathbf{k},\omega)e^{i(k\cdot r-\omega t)}d\mathbf{k}d\omega \quad (4)$$

$$\varphi(\mathbf{r},z,t) = \int \varphi(\mathbf{k},\omega)e^{[kz+i(k\cdot r-\omega t)]}d\mathbf{k}d\omega. \quad (5)$$

The variables $\eta(\mathbf{k}, \omega)$, $\varphi(\mathbf{k}, \omega)$, and ω are now expanded to third order. Thus $\eta = \eta_1 + \eta_2 + \eta_3$, $\varphi = \varphi_1 + \varphi_2 + \varphi_3$, and $\omega = \omega_o + \omega_1 + \omega_2$. Then Weber and Barrick solve equations (1)–(3) to various orders. To first order, they find

$$k\varphi_1(\mathbf{k},\omega) = -i\omega_o\eta_1(\mathbf{k},\omega) \quad (6)$$

and

$$-i\omega_o\varphi_1(\mathbf{k},\omega) = -g\eta_1(\mathbf{k},\omega) \quad (7)$$

which implies that

$$\mathbf{v}_1 = (\mathbf{a}_k - i\mathbf{a}_z)\omega_o\eta_1(\mathbf{k},\omega)$$

where $\mathbf{a_k}$ and $\mathbf{a}_z$ are unit vectors in the $\mathbf{k}$ and z directions, respectively, and that

$$\left(\omega_o^2 - gk\right)\eta_1(\mathbf{k},\omega) = 0$$

If $\eta_1$is not to be identically zero, then the waves must lie on the first-order dispersion relation:

$$\omega_o^2 = gk$$

In the region of ω/k space away from this first order dispersion curve, η_1 is zero but higher-order terms can exist. To avoid confusion, we define the wave number and angular frequency in this region to be Ω and $\mathbf{K}$, as did Weber and Barrick. Then the expansion of frequency in this region is $\Omega = \Omega_o + \Omega_1 + \Omega_2$.

[13] The second-order solutions are given by Weber and Barrick's equations 20 and 21, which may be combined to yield

$$\eta_2(\mathbf{k},\Omega) = \int A \;\; \eta_1(\mathbf{k},\omega)\eta_1(\mathbf{K}-\mathbf{k},\Omega-\omega)d\mathbf{k}d\omega \quad (8)$$

where

$$A = \frac{-\Omega_o\omega_o K(a_k\cdot a_K) + \omega_o^2 K + 0.5\omega_o K(\Omega_o-\omega_o)(1-a_k\cdot a_{k'})}{gK-\Omega_o^2} \quad (9)$$

and

$$v_2(\mathbf{K},\Omega) = (\mathbf{a}_K + i\mathbf{a}_z)\int B \;\; v_1(\mathbf{k},\omega)v_1(\mathbf{K}-\mathbf{k},\Omega-\boldsymbol{\omega})d\mathbf{k}d\omega \quad (10)$$

where B is

$$B = \frac{gK^2(\mathbf{a_k}\cdot\mathbf{a_K}) - \Omega_o\omega_o K - 0.5\Omega_o(\Omega_o-\omega_o)(1-\mathbf{a_k}\cdot\mathbf{a_{k'}})}{(\Omega_o-\omega_o)\left(gK-\Omega_o^2\right)} \quad (11)$$

where $\boldsymbol{a_{k'}} = (\boldsymbol{K} - \boldsymbol{k})/|\boldsymbol{K} - \boldsymbol{k}|$. Note that, Ω_o^2 and Ω^2 are not equal to gK in the second order equations. However, since $\eta_1(\boldsymbol{k}, \omega)$ and $v_1(\boldsymbol{k}, \omega)$ only exist on the first-order dispersion relation, we must still satisfy $\omega^2 = gk$ and $(\Omega - \omega)^2 = g|\boldsymbol{K} - \boldsymbol{k}|$.

3.2. Specialization to One Dimension

[14] The above equations are easier to interpret if we specialize to one dimension. Then $\boldsymbol{a_k} \cdot \boldsymbol{a_K} = \boldsymbol{a_k} \cdot \boldsymbol{a_{k'}} = 1$ and

$$\eta(k,\omega) = \eta_1(k,\omega) + \frac{K}{2}\int \;\; \eta_1(k,\Omega)\eta_1(K-k,\Omega-\omega) \;\; dkd\omega + \eta_3(k,\omega) \quad (12)$$

$$\mathbf{v}(k,\omega) = \mathbf{v}_1(k,\omega) + (\mathbf{a_K} + i\mathbf{a}_z)\frac{K}{2}\int \;\; Bv_1(k,\omega)v_1 \cdot (K-k,\Omega-\omega)dkd\omega + \mathbf{v}_3(k,\omega) \quad (13)$$

where

$$B = \frac{1}{\Omega_o - \omega_o} + \frac{\Omega_o}{gK - \Omega_o^2} \quad (14)$$

The terms η_3(k, ω) and $\mathbf{v}_3$(k, ω) represent third-order interaction terms, one example of which is an integral over a product of three first-order terms. When spectra of η and $\mathbf{v}$ are computed, these terms multiplied by η_1 are the same order as the square of η_2, the convolution terms above. They therefore yield a second-order correction to the spectrum which lies on the first-order dispersion curve. Spectra of the surface displacement, F, and of the horizontal component of surface velocity, V, therefore are given by

$$F(k,\omega) = \left(1 - k^2\langle\eta_1^2\rangle\right)F_1(k,\omega) + \frac{K^2}{2}\int \;\; F_1(k,\omega) \cdot F_1(K-k,\Omega-\omega)dkd\omega \quad (15)$$

$$V(k,\omega) = \left(1 - k^2\langle\eta_1^2\rangle\right)V_1(k,\omega) + \frac{K^2}{2}\int \;\; B^2V_1(k,\omega) \cdot V_1(K-k,\Omega-\omega)dkd\omega \quad (16)$$

where orthogonality of the Fourier components has been invoked and the terms involving $\langle\eta_1^2\rangle$ result from the third-order term given by *Creamer et al.* [1989]. Equation (16) can now be used to check these results against the radar data.

4. Comparisons With Radar Spectra

[15] If we filter the spectrum shown in Figure 1b so that only the first-order spectrum remains, we can divide it by the factor $(1 - k^2\langle\eta_1^2\rangle)$ to get V_1(k, ω). This can then be used in the convolution of equation (16) to obtain the theoretically predicted second-order spectrum, which can then be compared with the parts of the spectrum shown in Figure 1 that are off the first-order dispersion relation. Also, since the current and ship speed were not zero during the measurements, we now have

$$\omega = \pm\left[\sqrt{gk} + kU\right] \;\; \text{and} \;\; \Omega - \omega = \pm\left[\sqrt{g|K-k|} + |K-k|U\right] \quad (17)$$

where U incorporates both the current and ship speed.

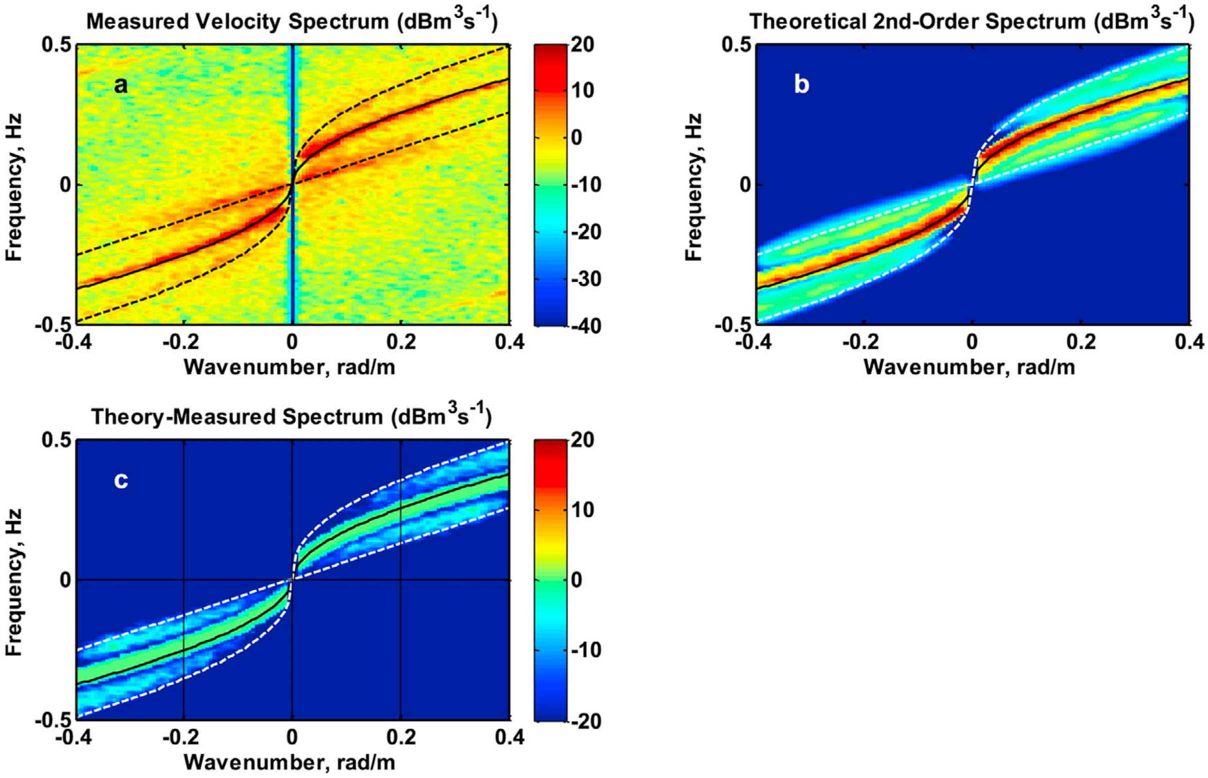

Figure 3. (a) The same measured wave number-frequency spectrum of scatterer velocity as shown in Figure 1a. (b) Second-order spectra computed using the first-order part of Figure 3a and equation (18). (c) The ratio (difference on a log scale) of the second-order spectra shown in Figures 3a and 3b, measured divided by computed. Solid lines show the first-order dispersion relation while dashed lines show the location of the measured features above and below the first-order relation.

[16] Then if we carry out the squaring of B, the convolution in equation (16) can be written

$$\begin{aligned}V_2(K,\Omega) &= \frac{K^2}{2}\int B^2 V_1(k,\omega)V_1(K-k,\Omega-\omega)dk\,d\omega \\ &= \frac{K^2}{2}\int V_1(k,\omega)\left\{\frac{V_1(K-k,\Omega-\omega)}{\left[\sqrt{g|K-k|}+|K-k|U\right]^2}\right\}dk\,d\omega \\ &\pm\frac{K^2\Omega_o}{gK-\Omega_o^2}\int V_1(k,\omega)\left\{\frac{V_1(K-k,\Omega-\omega)}{\sqrt{g|K-k|}+|K-k|U}\right\}dk\,d\omega \\ &+\frac{K^2}{2}\left\{\frac{\Omega_o}{gK-\Omega_o^2}\right\}^2\int V_1(k,\omega)V_1(K-k,\Omega-\omega)dk\,d\omega,\end{aligned} \tag{18}$$

which can now be evaluated. The plus sign in the third term of equation 18 is the relevant sign since both ω and k are positive on the first-order dispersion relation of the data. We note that the spectra computed from the radar data are V(k, f) where f = $\omega/(2\pi)$. Thus the spectrum shown in Figure 1 is related to V(k, ω) by V(k, f) = 2πV(k, ω). Then,

$$V(k,f) = \left(1-k^2\langle\eta_1^2\rangle\right)V_1(k,f)+V_2\left(K,\frac{\Omega}{2\pi}\right) \tag{19}$$

is the spectrum to be compared with the radar spectrum. Following Weber and Barrick, K and Ω are zero in the region of the wave number-frequency plane where $V_1 \neq 0$.

[17] Figure 3 shows the result of this operation compared with the measured second-order spectra. The computed spectra are clearly much smaller than the measured ones. Furthermore, the dashed lines in Figure 3b, which are the locations of the center of the measured features, show that the computed spectra lie closer to the first-order dispersion relation than is measured and that no straight line can be fit through them. Thus it appears that the predicted second-order spectra do not agree with the data.

[18] Another indication that second-order wave-wave interactions do not explain the low-frequency feature is the fact that we observed such a feature when looking nearly crosswind. Figure 4 shows a wave number-frequency spectrum from the radar when the antenna was pointing toward the east, nearly perpendicular to the wind, which was from 329°T at 10 m/s. Two features of this spectrum are particularly interesting. First, the remnants of an earlier wind sea are seen propagating toward the east. This swell has a wavelength around 95 m. Also observed in the spectrum is a low-frequency feature similar to those seen looking upwind (Figure 1a) but with smaller slope (lower speed) and propagating to the west, opposite the direction of the swell. Since the look direction is nearly perpendicular to the wind waves, their amplitude is so small that they do not show up along the first-order dispersion relation.

[19] We therefore conclude that second-order wave-wave interactions cannot explain the observations either when the

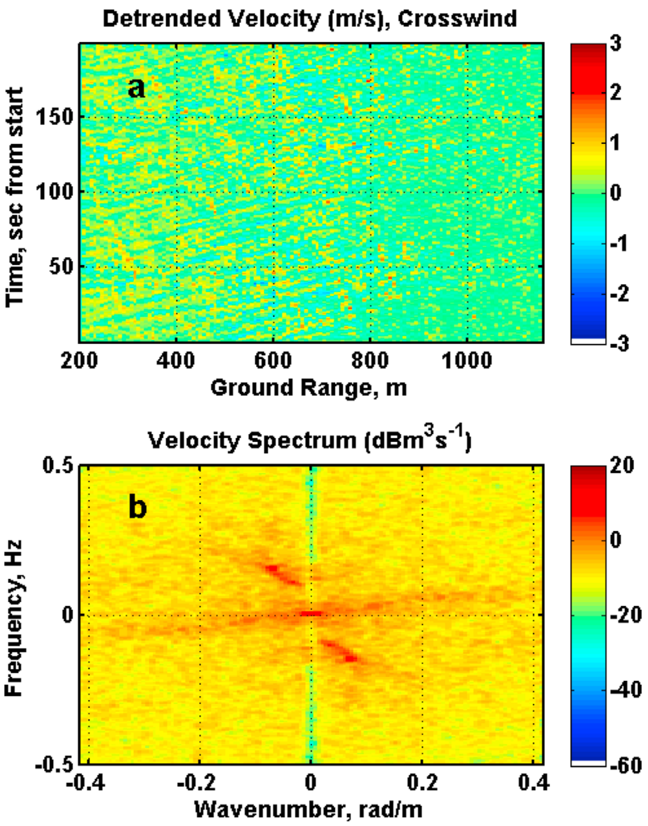

Figure 4. (a) Image of horizontal surface velocities obtained from a shipboard, coherent, X-band radar starting at 00:05:57 UTC on August 17, 2008. The polarization was VV. (b) The spectrum of this image showing swell traveling away from the radar and a linear feature traveling toward it. The data have been detrended. The wind velocity was 10.0 m/s from 329°T, the ship velocity was 0.6 m/s to 314°T, and the antenna was looking toward 45°T, nearly crosswind. The speed of the low-frequency feature is 1.5 m/s. The peak of the swell spectrum is at k = 0.0676 rad/m, or a wavelength of 93 m. Its frequency is 0.134 Hz for a period of 7.5 s. Thus it was traveling at 12.4 m/s.

antennas are directed nearly upwind or crosswind. Furthermore, since second-order scattering effects will have the same convolution form, they will also be located in the wrong place in the wave number-frequency spectrum and also cannot explain the observations.

5. Possible Shadowing Effects

[20] We now consider whether shadowing is the cause of these features. To investigate this we used a data set not taken in the experiment described above but carried out with a very similar radar. These data were collected in 1995 on the U.S.-LTA 138S airship using an X-band Doppler radar operated at HH polarization; the radar and experiment are described in detail by *Weissman et al.* [2002]. The airship flew at an altitude of 240 m so the range of grazing angles for this data set was 25.6° to 53.1°. Shadowing, of course, cannot occur at these grazing angles. For the data presented here, the radar antenna was fixed looking toward the front of the airship (which was moving backward). Space-time images of the detrended line-of-sight velocity measured by the radar, along with corresponding wave number-frequency spectra are shown in Figure 5.

[21] Clearly the low-frequency feature is observed in this spectrum even though shadowing does not occur. The speed of the linear feature is about 2.3 m/s in the frame of reference moving with the airship. The speed of the airship was 1.1 m/s in a downwind direction. Thus in the ground frame the linear feature is moving at about 3.5 m/s, similar to that of the data in Figure 1. The wind wave spectral peak is at k = 0.114 rad/m, or a wavelength of 55 m. Its frequency is 0.166 Hz for a period of 6 s. Therefore its velocity is 9.1 m/s in the airship frame of reference or about 10.2 m/s in the ground frame. The expected phase speed of a 55 m long wave is 9.3 m/s so a current component of about 0.9 m/s in the wind direction is indicated.

[22] The fact that the low-frequency feature is present even when shadowing cannot occur clearly indicates that shadowing cannot be the only cause of this feature at lower grazing angles. In fact, Plant and Farquharson (submitted manuscript, 2012) have shown that shadowing is unlikely to occur at all for VV polarization (as used in the shipboard measurements) and is questionable at best for HH polarization on the open ocean. We therefore discount shadowing as a source of the linear feature.

6. Interference Patterns

[23] Since neither wind turbulent eddies moving over the ocean surface at the mean wind speed nor water turbulence carried by currents nor second-order interactions can account for the observed features of the images and spectra, and shadowing effects are questionable at best, especially at VV polarization, we must search elsewhere for the cause of the features observed in our VV polarized data. Wind waves in the area of our measurements coexisted with swell coming from the west. We therefore consider a scenario where the wind waves and swell interfere and produce breaking near the points where the surface slope is particularly large.

[24] We simulate the surface displacements on the sea surface by first converting the ocean wave variance spectra of *Donelan et al.* [1985] from frequency to wave number as done by *Plant* [2002] to get F(k, φ). The wave number range was limited to 0.0184 to 0.362 rad/m in steps Δk = 0.0061 rad/m. The azimuth angle φ from the wind direction went from $-\pi$ to π in steps $\Delta\varphi$ = 0.0982 rad. Wind-wave amplitudes were computed from

$$A(k,\varphi) = 4\Gamma_1 * \sqrt{F(k,\varphi-\varphi_o)k\Delta k\Delta\varphi}$$

where φ_o is the angle of the wind with respect to north, Γ_1 is a Gaussian random variable with mean equal to 1 and variance equal to 0.2 and the factor of 4 was required to make wave amplitudes correspond to those observed by buoys deployed from the ship. Randomizing the amplitudes made little difference in the results presented here but was included to more accurately simulate a stochastic surface. We took the wind speed to be 7.5 m/s as in the data of Figure 1 and the fetch to be 500 km, which gave a peak

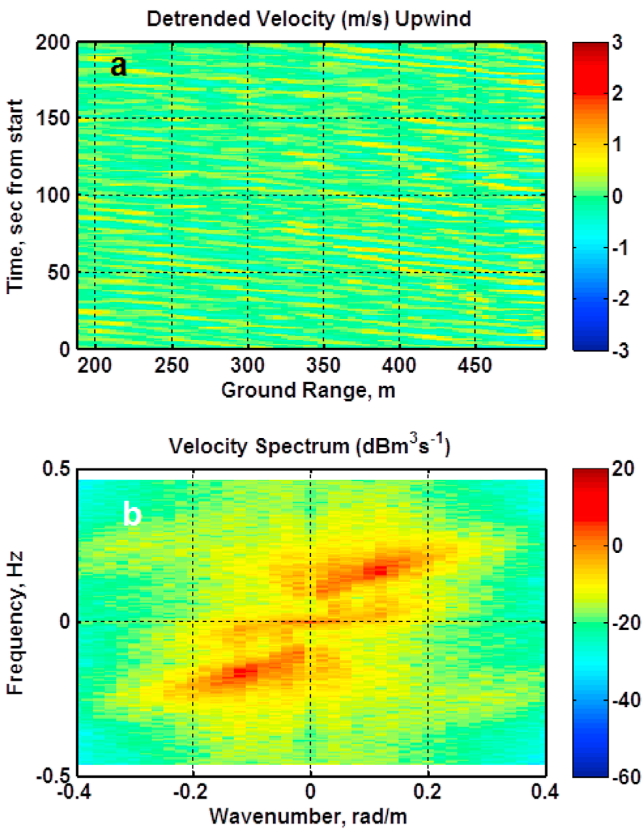

Figure 5. Coherent X-band radar data collected on an airship at grazing angles from 25.6° to 53.1°. (a) Image of line-of-sight surface velocities starting at 18:28:39 UTC on September 26, 1995. (b) The spectrum of this image. The wind velocity was 12.7 m/s from 176°T, the airship velocity was 1.1 m/s toward 320°T, and the antenna was looking toward 183°T, upwind. The airship heading was toward 176°T so the airship was being blown backward. HH polarization was used. The speed of the linear feature is 2.3 m/s in the airship's frame of reference or 3.5 m/s in ground coordinates.

wavelength of 68 m in good agreement with that observed in the data. Then two-dimensional wind-wave surfaces were generated for 128 times separated by one second from the equations

$$\gamma_i(\mathbf{x}, t_i) = \sum_j A(\mathbf{k}_j) \cos(\mathbf{k}_j \cdot \mathbf{x} - \omega t_i + \varphi_r(\mathbf{k}_j))$$

where φ_r is a random variable uniformly distributed between $-\pi$ and π. In a similar manner, horizontal and vertical velocities of the wavefield were computed from the equations

$$u_i(\mathbf{x}, t) = \sum_j \omega(\mathbf{k}_j) A(\mathbf{k}_j) \cos(\mathbf{k}_j \cdot \mathbf{x} - \omega t_i + \varphi_r(\mathbf{k}_j))$$

$$v_i(\mathbf{x}, t) = \sum_j \omega(\mathbf{k}_j) A(\mathbf{k}_j) \sin(\mathbf{k}_j \cdot \mathbf{x} - \omega t_i + \varphi_r(\mathbf{k}_j))$$

and the line-of-sight components in the north and east directions were computed:

$$V^i_{los} = \cos\varphi \sin\theta \; u_i(x, t) + \cos\theta \; v_i(x, t)$$

$$U^i_{los} = \sin\varphi \sin\theta \; u_i(x, t) + \cos\theta \; v_i(x, t)$$

The swell amplitude was taken to be a narrow-band, Gaussian, $2\Delta k$ wide distributed around the swell wavelength. It was considered to be unidirectional and its amplitude was multiplied by a Gaussian random variable with mean equal to 1 and variance equal to 0.1. Then two-dimensional swell surfaces for the amplitude, A_{si}, and two line-of-sight velocities, U^i_s and V^i_s, were generated for 128 times separated by one second. The swell amplitude was determined by setting its slope equal to 0.025 except when it was taken to be zero.

[25] Finally complete surfaces were generated by adding wind-wave and swell components together

$$\gamma_{tot}{}^i = \gamma_i + \gamma_{si}$$

$$V_{tot}{}^i = V_{los}{}^i + V_s{}^i \quad U_{tot}{}^i = U_{los}{}^i + U_s{}^i$$

From each γ^i_{tot}, the derivatives in the north and east directions were computed and pixels where this slope was below $-\tan 13°$ were found. We then added $3.5\Gamma_2$ to V^i_{tot} or U^i_{tot} if the north or east slope exceeded this threshold. Here Γ_2 is a Gaussian random variable with mean equal to 1 and variance equal to 1. In this manner, we attempted to account for breaking of short gravity waves where the magnitude of the slope of the larger scale surface on their front faces was large.

[26] Figure 6 shows the results of these simulations. We let the dominant wind wave come from 330 degT, the wind speed be 7.5 m/s, the swell come from 280 degT, and the incidence angle be 88°. Figure 6a shows the space-time image for a cut through the image stack in the northerly direction with the antenna nearly looking into the wind waves. The cut through the image was 352 m wide and the spatial variation in the look direction was an average over this perpendicular distance. The figure clearly shows the dominant wind waves with a modulation pattern superimposed on them. Pattern maxima move at about 3.2 m/s, very similar to the speeds of the modulation pattern shown in the actual data of Figure 1. Figure 6c shows the wave number-frequency spectrum of the space-time image of Figure 6a. The features of interest may be observed above and below the first-order dispersion relation. The low-frequency feature is a nearly straight line with a slope indicating the same speed of 3.2 m/s as the modulation pattern in the space-time image. Furthermore, the intensity of this feature relative to the energy on the first-order dispersion relation is about the same as that shown in Figure 1b for the data. Figure 6b shows a cut through the image stack in the easterly direction with the antenna looking east but with the dominant wind wave from 30 degT. Again wave features are visible, this time from the swell, as evidenced by the direction of propagation. A modulation pattern is also seen in Figure 6b that is steeper and less intense than the pattern in Figure 6a. Its slope yields a speed of 1.5 m/s. Figure 6d shows the wave number-frequency spectrum of the data of Figure 6b. The swell is now clearly seen on the first-order dispersion relation propagating away from the antenna but no trace of the wind-wave system is seen. The modulation pattern moves toward the antenna at a speed of 1.5 m/s. This wave number-frequency spectrum is very similar to that shown in Figure 4b, which was calculated from the data.

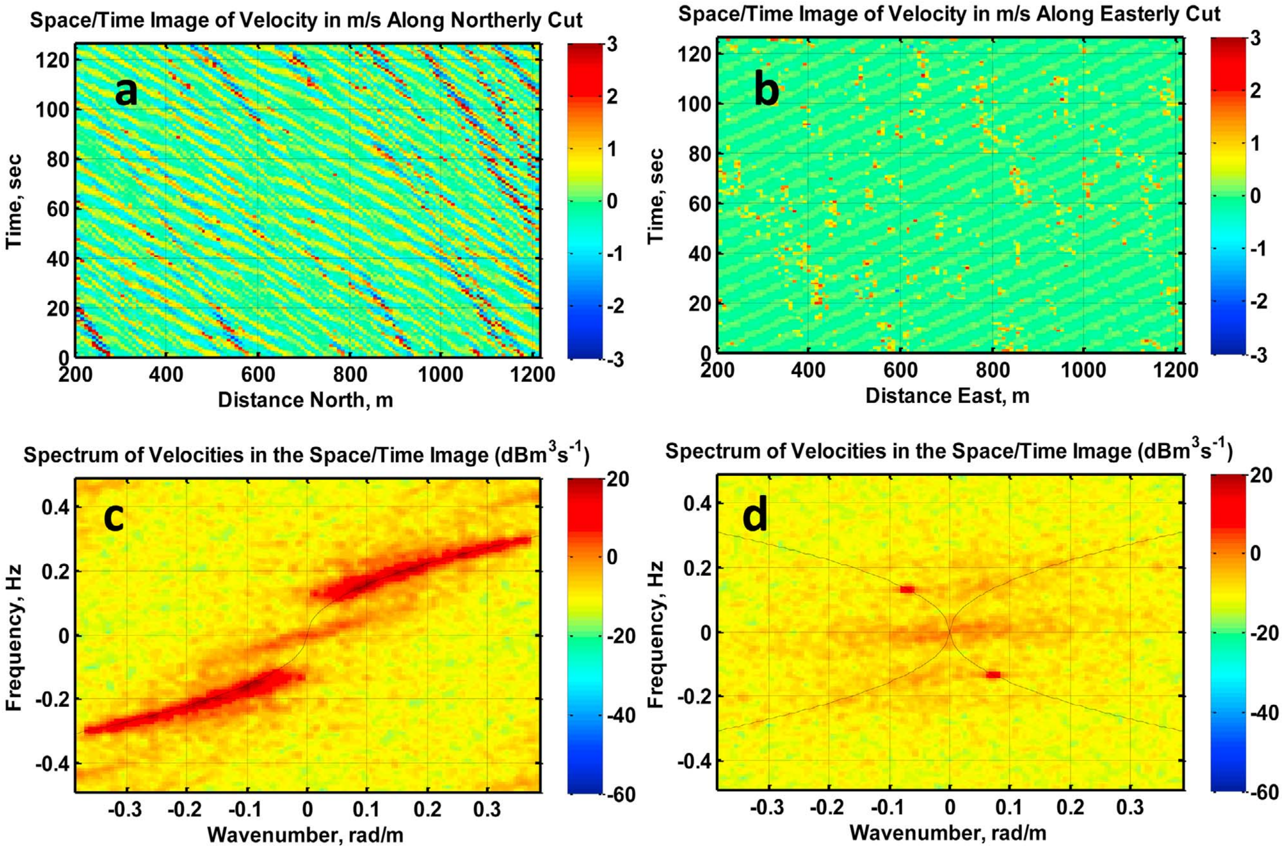

Figure 6. Results of simulating line-of-sight velocities observed by Doppler radars. (a) Space-time image of a cut through the image stack in the northerly direction. Antenna looks north, wind from 330 degT, swell from 280 degT. The speed of the modulation pattern is 3.2 m/s. (b) Space-time image of a cut through the image stack in the easterly direction. Antenna looks east, wind from 30 degT, swell from 280 degT. The speed of the modulation pattern is 1.5 m/s. (c) Wave number-frequency spectrum of the space-time image of Figure 6a. The slope of the linear, low-frequency feature indicates a speed of 3.2 m/s. (d) Wave number-frequency spectrum of the space-time image of Figure 6b. The slope of the low-frequency linear feature indicates a speed of 1.5 m/s and a propagation direction opposite that of the swell.

[27] We have investigated the cause of the modulation patterns observed in the space-time images and the corresponding low-frequency features in the wave number-frequency spectrum. If the wind direction is changed to 330 degT, the slope of the low-frequency feature in Figure 6d changes sign. If no wave breaking is added to the velocity images, the modulation patterns are still observed in the space-time images due to the interference of the long waves. As expected, however, no linear feature is seen in the wave number-frequency spectrum because no nonlinear interactions are taking place. If the swell amplitude is set to zero, both the modulation pattern and the low-frequency feature are still observed, although at a slightly reduced intensity. All of this leads us to conclude that the most likely cause of features observed in wave number-frequency spectra of ocean image stacks at locations other than those of the first-order dispersion relation is the breaking of waves caused by interference of wind waves either with themselves or with swell. Thus these features should be nearly universal at sufficiently high wind speeds. In the next section we show why we believe that short gravity waves rather than the dominant wind waves or swell are the breaking waves.

7. Doppler Velocities

[28] To attempt to determine whether Doppler shifts corresponding to breaking dominant wind waves occurred on the ocean, we looked at recorded Doppler spectra taken with the antenna looking upwind and downwind. *Stansell and MacFarlane* [2002] have recently shown in laboratory experiments that water parcel velocities produced by breaking waves are somewhat smaller than the linear phase speed of the breaking waves. They found mean parcel velocities to be between 0.81 and 0.95 times the phase speed, depending on the type of breaking. Thus, if dominant ocean waves were indeed the breaking waves, they would produce Doppler shifts corresponding to velocities that were within 80% of the dominant wave phase speed.

[29] During our data collection we computed and stored complete Doppler spectra at 14 range bins for each of the 1000 scans that were collected into individual files. For all of these spectra, we determined the highest frequency at which

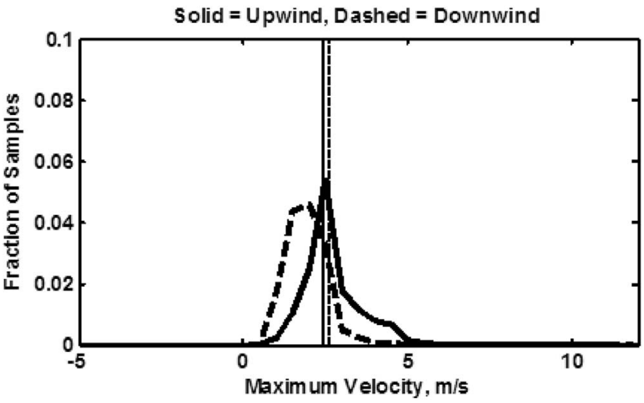

Figure 7. Histogram of the velocities of scatterers that were the fastest scatterers in Doppler spectra observed with antennas looking upwind or downwind. The solid curve is the histogram looking upwind while the dashed curve is the histogram looking downwind. Solid and dashed vertical lines show the speeds of linear features observed in wave number-frequency spectra of space-time images from the radar. The wind speed was 9.8 m/s.

the spectral density of the Doppler spectra exceeded the noise level by 10 dB or more. Our Nyquist frequency corresponded to a velocity of 12.5 m/s so we could unambiguously identify scatterers traveling at line-of-sight velocities up to this value. Figure 7 shows histograms of the maximum horizontal velocities obtained from each of the 14,000 spectra collected looking upwind and downwind with our VV polarized antennas. The largest horizontal velocity observed was 6 m/s while only 0.5% of the spectra showed horizontal velocities above 5 m/s. Thus the fastest scatterer would have been produced by a breaking wave whose linear phase speed was less than about 7 m/s. The peaks of the surface wave spectrum during our measurement period corresponded to surface waves whose linear phase speed was 11 to 12 m/s. Thus the waves that are breaking cannot be the dominant waves but must be shorter surface gravity waves that are steepened by currents set up by the interference patterns within the wind wave system.

8. Discussion

[30] In general, any process producing nonlinearities in space-time images can cause features to appear off the first-order dispersion relation in wave number-frequency spectra. In particular, clipping of intensity images can cause such features. This is why we have avoided using our images of radar cross section in this study. However, such processing-induced nonlinearities are not the only possible cause of the features in intensity images. *Dugan and Piotrowski* [2003, 2012] have convincingly shown that advection of sediments by turbulence in rivers and inlets can produce the features in optical images.

[31] However, on the open ocean or on large bodies of water with little current, these features appear to be produced by breaking waves. *Thomson and Jessup* [2009] observed such features in wave number-frequency spectra of video imagery of breaking waves on Lake Washington in Washington state. They used the low-frequency feature to deduce the properties of the crest length of breaking waves per unit area as a function of breaking speed, $\Lambda(c)$, introduced by *Phillips* [1985]. They found that $\Lambda(c)$ peaked at breaker speeds between 1 and 2, in agreement with *Thomson et al.* [2009] who used more conventional techniques for determining $\Lambda(c)$ on the same lake. On the open ocean, *Phillips et al.* [2001] and *Gemmrich et al.* [2008] found a similar behavior of $\Lambda(c)$ but peaking at slightly higher breaker speeds, about 3.5 m/s.

[32] It is interesting to note that the value of breaker speed found by Phillips *et al.* and Gemmrich *et al.* at the peak of $\Lambda(c)$ is nearly identical to peak of the scatterer speed found in our histograms of maximum Doppler velocities when looking upwind (Figure 7). In fact, it is tempting to try to extract $\Lambda(c)$ from these measurements of Doppler velocities in the same manner that Thomson and Jessup did. However, they were able to calibrate their values by looking at images to determine the total crest length contained in each one. We are not able to do this with the microwave data.

[33] It is also interesting to note that our conclusion that the most likely breaking waves on the ocean are short-gravity waves is very similar to the conclusion drawn by many investigators looking at microwave sea spikes at low-grazing angles [*Lee et al.*, 1995; *Liu et al.*, 1998; *Frasier et al.*, 1998] and at high-incidence-angle microwave backscatter from the ocean [*Smith et al.*, 1996; *Plant*, 1997]. In all of these studies, the most likely breaking waves on the ocean were shown to be waves much shorter than the dominant waves on the ocean. Figure 7 shows that the peak of the upwind histogram agrees well with the speed of the low-frequency feature in the wave number-frequency spectrum in the upwind direction shown in Figures 1b and 6c. We have exercised our simulation of the low-frequency feature and found that for shorter dominant wavelengths, the speed indicated by this feature decreased. This is in line with the difference in breaker speed at the peak of $\Lambda(c)$ found by Thompson and Jessup on a lake and by Gemmrich *et al.* on the ocean. We are led to hypothesize that the short-wave breaking is induced by long-wave interference. The pattern of interference moves along in a manner similar to the currents in an internal wave and these have been shown to steepen short-gravity waves of nearly the speeds our maximum Doppler velocities [*Thompson*, 1988; *Plant et al.*, 2010].

9. Conclusions

[34] We have shown that neither turbulent eddies in the wind traveling at the mean wind speed nor water turbulence advected by currents nor second-order interactions due to either hydrodynamic or electromagnetic nonlinearities can cause the low-frequency feature found in wave number-frequency spectra of remotely sensed ocean images. Shadowing, if it exists, can cause such features but cannot be the only cause since the feature exists in spectra obtained at high grazing angles. In any case, evidence that shadowing is the cause is questionable. On the other hand, simulations of wave surfaces that include wave breaking at maximum slopes of the wind-wave interference pattern produce both the low-frequency feature and the high-frequency features usually observed below and above the first-order dispersion curve. Furthermore, such interference-induced wave breaking can

also account for the low-frequency feature observed in our nearly crosswind wave number-frequency spectra that travels in the opposite direction to the swell. Doppler spectra recorded by our X-band Doppler radar showed no evidence of scatterers traveling faster than 6 m/s even though the dominant wave linear phase speed was 11 to 12 m/s. Our conclusion is that the most common origin of features seen off the first-order dispersion relation in wave number-frequency spectra of remotely sensed space-time images on the open ocean is the breaking of short gravity waves on the surface due to large current gradients or slopes caused by the interference of dominant surface waves. This conclusion agrees well with that of *Irisov and Voronovich* [2011] who found in a numerical study that short gravity waves on the ocean break due to local maxima of current convergence or steepness.

[35] **Acknowledgments.** This study was made possible by several grants from the Office of Naval Research (ONR) including NNX11AL27G, F012919, and APS-11-12. Grant A100747 from the Bureau of Ocean Energy Management (BOEM) enabled the study to be completed.

References

Barrick, D. E., and B. L. Weber (1977), On the nonlinear theory for gravity waves on the ocean's surface. Part II. Interpretation and applications, *J. Phys. Oceanogr.*, *7*, 11–21, doi:10.1175/1520-0485(1977)007<0011:OTNTFG>2.0.CO;2.

Creamer, D. B., F. Henyey, R. Schult, and J. Wright (1989), Improved linear representation of ocean surface waves, *J. Fluid Mech.*, *205*, 135–161, doi:10.1017/S0022112089001977.

Donelan, M. A., J. Hamilton, and W. H. Hui (1985), Directional spectra of wind generated waves, *Philos. Trans. R. Soc. London, Ser. A*, *315*, 509–562, doi:10.1098/rsta.1985.0054.

Dugan, J. P., and C. C. Piotrowski (2003), Surface current measurements using airborne visible image time series, *Remote Sens. Environ.*, *84*, 309–319, doi:10.1016/S0034-4257(02)00116-5.

Dugan, J. P., and C. C. Piotrowski (2012), Measuring currents in a coastal inlet by advection of turbulent eddies in airborne optical imagery, *J. Geophys. Res.*, *117*, C03020, doi:10.1029/2011JC007600.

Dugan, J. P., C. C. Piotrowski, and J. Z. Williams (2001), Water depth and surface current retrievals from airborne optical measurements of surface gravity wave dispersion, *J. Geophys. Res.*, *106*(C8), 16,903–16,915, doi:10.1029/2000JC000369.

Frasier, S. J., and R. E. McIntosh (1996), Observed wavenumber-frequency properties of microwave backscatter from the ocean surface at near-grazing angles, *J. Geophys. Res.*, *101*(C8), 18,391–18,407, doi:10.1029/96JC01685.

Frasier, S. J., Y. Liu, and R. E. McIntosh (1998), Space-time properties of radar sea-spikes and their relation to wind and wave conditions, *J. Geophys. Res.*, *103*(C9), 18,745–18,757, doi:10.1029/98JC01456.

Gemmrich, J. R., M. L. Banner, and C. Garrett (2008), Spectrally resolved energy dissipation rate and momentum flux of breaking waves, *J. Phys. Oceanogr.*, *38*, 1296–1312, doi:10.1175/2007JPO3762.1.

Hasselmann, K. (1962), On the non-linear energy transfer in a gravity-wave spectrum: Part 1. General theory, *J. Fluid Mech.*, *12*, 481–500, doi:10.1017/S0022112062000373.

Hasselmann, K. (1963), On the non-linear energy transfer in a gravity-wave spectrum: Part 3. Evaluation of the energy flux and swell-sea interaction for a Neumann spectrum, *J. Fluid Mech.*, *15*, 385–398, doi:10.1017/S002211206300032X.

Irisov, V., and A. Voronovich (2011), Numerical simulation of wave breaking, *J. Phys. Oceanogr.*, *41*, 346–364, doi:10.1175/2010JPO4442.1.

Lee, P. H. Y., J. D. Barter, K. L. Beach, C. L. Hindman, B. M. Lake, H. Rungaldier, J. C. Shelton, A. B. Williamn, R. Yee, and H. C. Yuen (1995), X band microwave backscattering from ocean waves, *J. Geophys. Res.*, *100*, 2591–2611, doi:10.1029/94JC02741.

Liu, Y. S. J., S. J. Frasier, and R. E. McIntosh (1998), Measurements and classification of low-grazing-angle radar sea spikes, *IEEE Trans. Antennas Propag.*, *46*(1), 27–40, doi:10.1109/8.655448.

Longuet-Higgins, M. S. (1962), Resonant interactions between two trains of gravity waves, *J. Fluid Mech.*, *12*, 321–332, doi:10.1017/S0022112062000233.

Phillips, O. M. (1960), On the dynamics of unsteady gravity waves of finite amplitudes. Part 1. The elementary interactions, *J. Fluid Mech.*, *9*, 193–217.

Phillips, O. M. (1985), Spectral and statistical properties of the equilibrium range in wind-generated gravity waves, *J. Fluid Mech.*, *156*, 505–531, doi:10.1017/S0022112085002221.

Phillips, O. M., F. L. Posner, and J. P. Hansen (2001), High range resolution radar measurements of the speed distribution of breaking events in wind-generated ocean waves: Surface impulse and wave energy dissipation rates, *J. Phys. Oceanogr.*, *31*, 450–460, doi:10.1175/1520-0485(2001)031<0450:HRRRMO>2.0.CO;2.

Plant, W. J. (1997), A model for microwave Doppler sea return at high incidence angles: Bragg scattering from bound, tilted waves, *J. Geophys. Res.*, *102*(C9), 21,131–21,146, doi:10.1029/97JC01225.

Plant, W. J. (2002), A stochastic, multiscale model of microwave backscatter from the ocean, *J. Geophys. Res.*, *107*(C9), 3120, doi:10.1029/2001JC000909.

Plant, W. J., W. C. Keller, A. B. Reeves, E. Uliana, and J. W. Johnson (1987), Airborne microwave Doppler measurement of ocean wave directional spectra, *Int. J. Remote Sens.*, *8*(3), 315–330, doi:10.1080/01431168708948644.

Plant, W. J., W. C. Keller, V. Hesany, and K. Hayes (1998), Measurements of the marine boundary layer from an airship, *J. Atmos. Oceanic Technol.*, *15*, 1433–1458, doi:10.1175/1520-0426(1998)015<1433:MOTMBL>2.0.CO;2.

Plant, W. J., W. C. Keller, K. Hayes, G. Chatham, and N. Lederer (2010), Normalized radar cross section of the sea for backscatter: 2. Modulation by internal waves, *J. Geophys. Res.*, *115*, C09033, doi:10.1029/2009JC006079.

Rino, C. L., E. Eckert, A. Siegel, T. Webster, A. Ochadlick, M. Rankin, and J. Davis (1997), X-band low-grazing-angle ocean backscatter obtained during LOGAN 1993, *IEEE J. Oceanic Eng.*, *22*(1), 18–26, doi:10.1109/48.557536.

Smith, M. J., E. M. Poulter, and J. A. McGregor (1996), Doppler radar measurements of wave groups and breaking waves, *J. Geophys. Res.*, *101*(C6), 14,269–14,282, doi:10.1029/96JC00766.

Stansell, P., and C. MacFarlane (2002), Experimental investigation of wave breaking criteria based on wave phase speeds, *J. Phys. Oceanogr.*, *32*, 1269–1283, doi:10.1175/1520-0485(2002)032<1269:EIOWBC>2.0.CO;2.

Stevens, C. L., E. M. Poulter, M. J. Smith, and J. A. McGregor (1999), Nonlinear features in wave-resolving microwave radar observations of ocean waves, *IEEE J. Oceanic Eng.*, *24*(4), 470–480, doi:10.1109/48.809268.

Thompson, D. R. (1988), Calculation of radar backscatter modulations from internal waves, *J. Geophys. Res.*, *93*(C10), 12,371–12,380, doi:10.1029/JC093iC10p12371.

Thomson, J., and A. T. Jessup (2009), A Fourier-based method for the distribution of breaking crests from video observations, *J. Atmos. Oceanic Technol.*, *26*, 1663–1671.

Thomson, J., J. R. Gemmrich, and A. T. Jessup (2009), Energy dissipation and the spectral distribution of whitecaps, *Geophys. Res. Lett.*, *36*, L11601, doi:10.1029/2009GL038201.

Van Vleck, J. H., and D. Middleton (1966), The spectrum of clipped noise, *Proc. IEEE*, *54*(1), 2–19, doi:10.1109/PROC.1966.4567.

Weber, B. L., and D. E. Barrick (1977), On the nonlinear theory for gravity waves on the ocean's surface. Part I: Derivations, *J. Phys. Oceanog.*, *7*, 3–10, doi:10.1175/1520-0485(1977)007<0003:OTNTFG>2.0.CO;2.

Weissman, D. E., W. J. Plant, W. C. Keller, and V. G. Irisov (2002), Comparison of scatterometer and radiometer wind vector measurements, *J. Atmos. Oceanic Technol.*, *19*, 100–113, doi:10.1175/1520-0426(2002)019<0100:COSARW>2.0.CO;2.